

VascX Models: Model Ensembles for Retinal Vascular Analysis from Color Fundus Images

Jose Vargas Quiros^{1,2}, Bart Liefers^{1,2}, Karin van Garderen^{1,2}, Jeroen Vermeulen^{1,2}, Eyened Reading Center^{1,2}, Sinergia Consortium^{1,5,6,7}, and Caroline Klaver^{1,2,3,4}

¹Department of Ophthalmology, Erasmus University Medical Center, Rotterdam, the Netherlands

²Department of Epidemiology, Erasmus University Medical Center, Rotterdam, the Netherlands

³Department of Ophthalmology, Radboud University Medical Center, Nijmegen, the Netherlands

⁴Institute of Molecular and Clinical Ophthalmology, University of Basel, Switzerland

⁵Department of Computational Biology, University of Lausanne, Lausanne, Switzerland

⁶Jules Gonin Eye Hospital (HOP), Fondation Asile des aveugles, Lausanne, Switzerland

⁷Department of Clinical Neuroscience, Lausanne University Hospital, Lausanne, Switzerland

ABSTRACT

We introduce VascX models, a comprehensive set of model ensembles for analyzing retinal vasculature from color fundus images (CFIs). Annotated CFIs were aggregated from public datasets for vessel, artery-vein, and disc segmentation; and fovea localization. Additional CFIs from the population-based Rotterdam Study were, with arteries and veins annotated by graders at pixel level. Our models achieved robust performance across devices from different vendors, varying levels of image quality levels, and diverse pathologies. Our models demonstrated superior segmentation performance compared to existing systems under a variety of conditions. Significant enhancements were observed in artery-vein and disc segmentation performance, particularly in segmentations of these structures on CFIs of intermediate quality, a common characteristic of large cohorts and clinical datasets. Our model outperformed human graders in segmenting vessels with greater precision. With VascX models we provide a robust, ready-to-use set of model ensembles and inference code aimed at simplifying the implementation and enhancing the quality of automated retinal vasculature analyses. The precise vessel parameters generated by the model can serve as starting points for the identification of disease patterns in and outside of the eye.

Keywords: vascx, vascular biomarkers, vascular features, medical image analysis, fundus segmentation, artery-vein segmentation, optic disc segmentation, fovea detection

INTRODUCTION

Interest in measuring retinal calibers dates back to the 1970s when Parr and Spears published their approach to approximate the caliber of the central retinal artery and vein using the calibers of their largest branches [28]. Since the late 1990s, various semi-automatic methods have been developed to perform these calculations with different levels of human and machine involvement, enhancing the efficiency of such measurements [17]. Among these developments were prominent tools such as SIVA (Singapore I Vessel Assessment) [38, 22, 20, 36, 6], IVAN [4, 5], and VAMPIRE (Vascular Assessment and Measurement Platform for Images of the Retina) [29, 33, 34].

Today the understanding of retinal vasculature and its association with diseases has expanded substantially. A significant focus has been placed on biomarkers such as retinal calibers, tortuosity, and branching characteristics. These biomarkers are now studied not only in relation to ocular diseases but also to systemic conditions, particularly cardiovascular diseases [37, 24]. More recently, attention has

turned to the retina as a window into brain pathology, with studies linking retinal vascular changes to neurodegenerative diseases such as Alzheimer’s disease [12].

Parallel to the scientific advances, deep learning brought about ground-breaking improvements in segmentation quality across a variety of tasks [19]. This triggered the development of multiple datasets and deep learning architectures for the segmentation of the main anatomical structures visible in CFIs: vessel segmentation, artery-vein segmentation, and disc segmentation [2]. More recent attempts to integrate these models into pipelines for fully automated vascular feature extraction. Automorph is the most notable example of a deep-learning-based pipeline integrating vessel segmentation, artery-vein segmentation, disc segmentation, and vascular feature extraction Zhou et al. [40]. Additionally, region-based analysis have been implemented to isolate features from specific areas of the retina, utilizing optic disc and fovea detection models. These approaches allow for a more granular analysis, offering a deeper understanding of the temporal development of retinal changes.

Despite these developments, automated segmentation of features on CFIs remains far from solved. Publicly available training datasets are small and homogeneous, often limited to images from a single device, centered on small anatomic regions like the fovea or optic disc, or with a narrow field of view. Until recently [35], the largest publicly available dataset [2] for artery-vein segmentation contained only 45 images. Additionally, the pathology and demographics of the study population are often restricted, which significantly impacts the generalizability of the models trained on these datasets. These limitations are particularly problematic in analyses of large cohort studies, which typically encompass a diverse range of devices and capture conditions. To overcome these drawbacks, large and diverse datasets are needed that allow the development of robust models that are effective and reliable across a broad spectrum of conditions. Annotations of vessel crossings should be optimized to ensure modeling of intact vessel tree connectivity.

In this paper, we present contributions towards a robust analysis of the retinal vasculature through improved segmentation and localization models. Our contributions are the following:

- We present models for optic disc, vessel, and artery-vein segmentation and fovea localization, fundamental models in the development of CFI analysis systems, especially of the retinal vasculature. We built our models using public datasets and new annotations by professional graders on diverse sets of CFIs from the Rotterdam Study.
- We benchmark our models against publicly available models [40, 15] and show significant improvements in segmentation performance. We characterize the performance of the models with respect to image quality as measured using our quality assessment model.
- We evaluate the quality of features extracted from model output by comparing them to features extracted from segmentations made by experienced graders.
- We publicly release and make open-source our pre-processing and inference code, including model weights.

METHODS

0.1 Datasets

We trained and evaluated our models on a combination of public datasets and images from the Rotterdam Study (RS).

0.1.1 Public Datasets

We collected publicly available datasets from previous work. These datasets have different patient demographics, pathologies, retinal regions (fovea and disc centered), capture devices, field of view and countries of origin. Table 1 shows an overview of these datasets.

We included several well-known vessel and artery-vein segmentation datasets with diabetic retinopathy (DR) patients [16, 2, 25, 3]. We excluded the DRIVE dataset [32, 31] due to its low resolution (584×565 pixels). We included the larger and more recent FIVES [21] and Leuven-Haifa [35] datasets, which contain a mixture of diseased and healthy patients. On the other hand, most disc segmentation datasets were originally collected for the assessment of glaucoma Zhang et al. [39], Kovalyk et al. [23], Fang et al. [9]. Exceptions are ADAM (age-related macular degeneration), PALM (pathological myopia) and IDRiD

Table 1. Overview of datasets for various segmentation and localization tasks. Pathologies: H: healthy, GC - glaucoma (all types), NTG: normal tension glaucoma, HTG: high tension glaucoma, HT: hypertension, DR: diabetic retinopathy, AMD: age-related macular degeneration, PM: pathological myopia, O: other eye diseases. * 379 of 1200 samples were discarded due to containing no disc segmentation for partially visible discs. ** 21 of 1200 CFIs were discarded due to having no associated annotation.

Dataset	N	Origin	Ages	Pathology	Region	FOV
Vessel Segmentation						
Chase DB [11]	28	UK	Children	-	OD	35°
DRHAGIS [16]	40	UK	NR	10 GC, 10 HT, 10 DR, 10 AMD	M	45°
HRF [2]	45	GER	NR	15 H, 15 DR, 15 GC	M	45°
RETA [25]	54	IND	NR	Signs of DR	M	50°
FIVES [21]	800	CN	4-83	H, GC, DR, AMD	M	50°
Leuven-Haifa [35]	240	BE	18-90	75 NTG, 63 HTG, 56H, 30 O	OD	30°
RS (ours)	352	NL	40+		See Figure 1.	
Total	1559					
Artery Vein Segmentation						
RITE [31]	40	NL	25-90	7 DR, 33 no DR	M	45°
HRF-AV [3]	45	GER	NR	15 H, 15 DR, 15 GC	M	45°
Les-AV [26]	22	NR	NR	NR	OD	30°
Leuven-Haifa [35]	240	BE	18-90	75 NTG, 63 HTG, 56H, 30 O	OD	30°
RS (ours)	215	NL	40+		See Figure 1.	
Total	562					
Disc Segmentation						
ORIGA [39]	650	SGP	40-80	Multiple	OD	NR
PAPILA [23]	488	SPN	15-90	87 GC, 333 H, 68 O	OD	30°
IDRiD [30]	81	IND	NR	Signs of DR	M	50°
ADAM [8]	821*	CN	53.2 ± 15.6	267 AMD, 933 O	M, OD, MP	45°
PALM [7]	1179**	CN	37.5 ± 15.91	637 PM, 563 O	M, OD, MP	45°
REFUGE2 [9]	2000	CN	NR	280 GC, 1720 H/O	M, OD, MP	45°
RS (ours)	1225	NL	40+		See Figure 1.	
Total	7464					
Fovea Localization						
IDRiD [30]	516	IND	NR	Signs of DR	M	50°
ADAM [8]	1200	CN	53.2 ± 15.6	267 AMD, 933 O	M, OD, MP	45°
PALM [7]	1200	CN	37.5 ± 15.91	637 PM, 563 O	M, OD, MP	45°
REFUGE2 [9]	2000	CN	NR	280 GC, 1720 H/O	M, OD, MP	45°
RS (ours)	10908	NL	40+		See Figure 1.	
Total	15824					
CFI Quality Estimation						
EyeQ [14]	28,792					

(diabetic retinopathy); which also contain fovea positions. Finally, we used the Eye-Quality (EyeQ) dataset for the quality estimation algorithm. This dataset is unique for its size and for containing a variety of capture devices and image conditions. The field-of-view of the images in our training set is between 30° and 50°, which includes the vast majority of standard fundus imaging devices.

0.1.2 Rotterdam Study Datasets

We complimented the CFI’s from the public data sets with randomly sampled CFIs from the Rotterdam Study (RS). This study is a prospective population-based cohort study of people living in Ommoord, a district of the city of Rotterdam (Ikram et al. [18]). The RS consists of four cohorts, all of which were used in this work. The minimum age of study participants varies between > 55 in the first cohort and > 40 in the fourth. Each cohort was followed for multiple rounds of follow-up examinations every 4 to 5 years. Most of the patient visits in the RS involved the capture of CFIs on both eyes. Due to the multi-decade span of the RS, multiple devices, capture conditions and fields (macula and disc centered) are present in the dataset. The RS is entered into the Netherlands National Trial Register (NTR) and the WHO International Clinical Trials Registry Platform (ICTRP) under shared catalog number NTR6831. All participants provided written informed consent following the Declaration of Helsinki to participate in the study and to have their information obtained from their treating physicians.

0.1.3 CFI Selection and Weighing

We used most public datasets in their entirety without filtering, after harmonizing annotations where necessary. The main exception were disc segmentations in the ADAM dataset, where 379 of 1200 samples were discarded due to containing no disc segmentation for partially visible discs.

Regarding the Rotterdam Study, we selected CFIs at random for the vessel and A/V segmentation datasets (Table 1), only excluding images that were deemed unusable due to low image quality. We used the quality estimation model in Automorph [40] to assess image quality. Additionally, we asked graders to exclude images for which they found the quality to be unusable for the task at hand.

For disc segmentation, due to the large size of publicly available datasets (Table 1), we used a model trained on publicly available datasets to automatically identify failure or challenging CFIs. We selected CFIs for which no disc was detected or a disconnected disc mask was produced by the model. A trained grader reviewed these images and identified the ones where the disc was present but incorrectly segmented, and these were included in the training set.

For fovea detection, we used CFIs from a RS sub-cohort graded for Age-related Macular Degeneration (AMD).

Figure 1 shows the statistics of the final Rotterdam Study CFI development sets. Vessel and artery-vein segmentation sets are similar (partly due to overlap) and are closer to the overall distribution of the RS. The disc segmentation dataset, on the other hand, contains more images from the analog devices, which were often the hardest to segment partly due to unconventional disc placement.

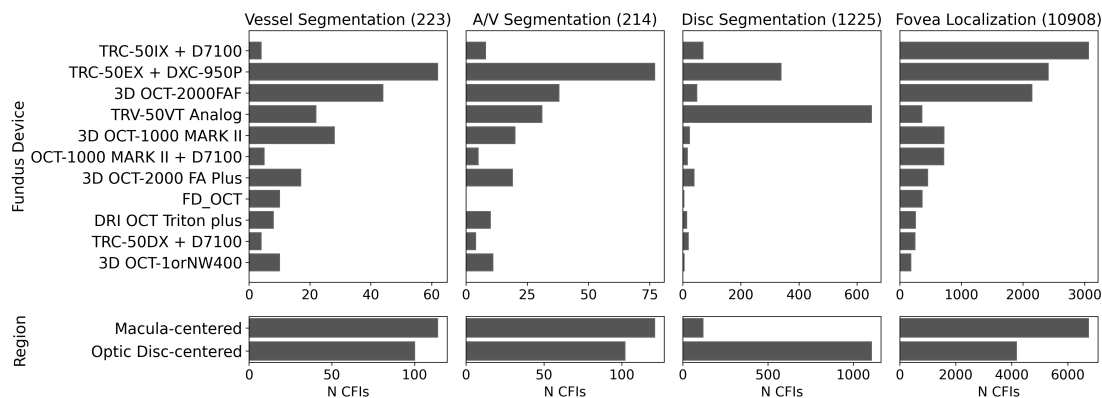


Figure 1. Statistics of the Rotterdam Study sets used to train VascX models.

0.2 CFI annotation

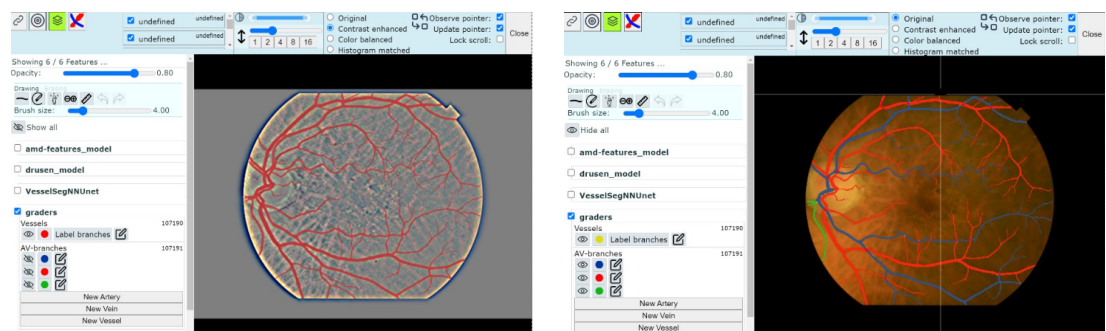
Images were annotated using custom software for ophthalmological image annotation. Four professional graders participated in the process. The graders worked on desktop computers with a drawing tablet for segmentation. The annotation process was different per annotation type:

Vessel segmentation For the first 100 images the interface was initialized with outputs from the publicly available model Automorph Zhou et al. [40]. The graders were instructed to independently fix the masks produced by the model, including missing vessels and over-segmentation. A digitally enhanced version of the image with increased contrast of vessel edges was used to aid the graders (Figure 2a). After this, a model trained on these annotations and the publicly available data was used in place of Automorph as initialization for the remaining images.

Artery-vein segmentation We resolved connectivity issues at artery-vein crossings by annotating arteries and veins on separate layers. An interface was developed specifically for artery-vein segmentation (Figure 2b) to allow the graders to start from a vessel segmentation and color arteries and veins into two independent masks or layers using drawing tools. A third layer - *Unknown* was added for vessels that could not be recognized as either. They were asked to color A/V crossings on both layers (overlapping). They were able to visualize and correct each layer independently, or all the same time. Another tool allowed them to visualize the connected components of each mask in different colors to easily find mistakes in connectivity. The entire process consisted in 1) correcting mistakes in the provided mask (vessel segmentation); 2) coloring the mask into A/V and unknown colors/layers; 3) Verifying connected components on the A/V masks and filling any gaps.

Disc segmentation A single professional grader performed this annotation using the same drawing interface used for binary vessel segmentation (Figure 2a). The grader colored the entire optic disc area excluding any peri-papillary atrophy (PPA) region to match the annotations on public datasets [1, 39, 13]. In cases of doubt due to poor image quality or unclear disc boundaries, a consensus was reached between the three graders. Cases where the image quality was too poor to reach consensus were excluded.

Fovea localization Four graders placed an ETDRS grid on the fundus image. The process consisted in clicking on the fovea center and on the optic disc border point closest to the fovea. These points were used to display a grid on top of the image, which could be corrected in case of mistakes.



(a) Vessel segmentation: graders corrected binary masks generated by AI, using a digitally contrast-enhanced image to visualize vessels.

(b) Artery-vein segmentation: graders colored the vessel masks into two separate (overlapping) masks for arteries and veins using a custom interface.

Figure 2. Screen capture of the software used for all the annotations on Rotterdam Study CFIs.

0.3 Model Training

We implemented an improved CFI bounds detection and pre-processing procedure and used well-known model architectures such as U-Net for model training.

0.3.1 Data pre-processing

For all models, training and testing CFIs were pre-processed via:

1. Detection of the CFI boundaries defined by a circle and top and bottom vertical padding.
2. Cropping of the CFI along its boundaries into a square image and resizing to $1024 \times 1024 \text{px}$.
3. Contrast enhancement via Gaussian filtering. The image was mirrored along its boundaries before contrast enhancement to avoid artifacts, and the region outside its boundaries was blacked out after enhancement.

The geometric steps above (cropping and resizing) were replicated on the labels for training.

0.3.2 Vessel and A/V segmentation models

Vessel and A/V segmentation models were trained separately given the different development sets. Data was augmented via random appearance transforms: de-focus, hue-saturation-value, Gamma and Gaussian noise; followed by geometric transforms: flipping (horizontal and vertical), random scale (1.0-1.15 times original scale) random rotation (up to 10 degrees), random elastic transforms and finally random cropping of a $512 \times 512 \text{px}$ patch. This was done to maintain enough resolution for the segmentation of the thinner vessels. Correspondingly, inference is done on $1024 \times 1024 \text{px}$ images via a sliding window with 50% overlap. A Gaussian kernel was used for merging window segmentations. Test-time augmentation was also applied: the outputs of horizontal, vertical, and horizontal-vertical flips were averaged together before binarizing the final output. These procedures closely follow or are inspired by the process followed in NN-UNet Isensee et al. [19].

Vessel annotations were encoded as 0) background and 1) vessel. Artery-vein annotations were encoded as 0) background, 1) arteries, 2) veins, and 3) crossings (both artery and vein). We used this approach with the goal of boosting the relative importance of the crossings in the loss function. The loss function was the weighted sum of Dice and Cross-entropy with equal weights.

The models were trained making use of a custom implementation of the U-Net with 6 input channels (for original RGB image and contrast-enhanced version), 8 down-sampling stages, and deep supervision (loss calculated on the down-sampled stages too). The input resolution was $512 \times 512 \text{px}$.

0.3.3 Fovea and disc localization models

The fovea and disc localization models were trained separately to localize keypoints on the CFIs. A heatmap regression approach was used using the same U-Net architecture used for artery-vein segmentation. Annotated keypoints were used to generate target heatmaps ($512 \times 512 \text{px}$) using a Gaussian centered at the keypoint location. The σ for the Gaussian was set via experiments on a different CFI localization task. Mean squared error (MSE) was used as loss function to train the model to approximate the continuous target heatmaps. The location (2D-index) of the maximum over the heatmaps output by the model was taken as the keypoint location.

Input CFIs were augmented via random appearance transforms: de-focus, hue-saturation-value, Gamma and Gaussian noise; followed by geometric transforms: horizontal flipping, random scale (1.0-1.05 times original scale) random rotation (up to 5 degrees) and finally resizing down to model input size. Test-time augmentation was correspondingly applied using the vertical flip of the input.

0.3.4 Quality classification model

The image quality classification model was trained using the same augmentations as for fovea and disc models. The models were developed by fine-tuning Resnet101 (Imagenet weights) with 224px input resolution. Here we used only the original RGB CFI (3 channels; no contrast-enhanced version). All the model weights were fine-tuned (no frozen layers). The cross-entropy loss was used for classification and Mean Squared Error (MSE) for regression. Test-time augmentation was applied by averaging the outputs of the original and horizontally-flipped inputs.

0.3.5 Training setup

For all models, we made use of the *albumentations* library for data augmentations. Pytorch and *pytorch-lightning* were used to develop our model training pipeline.

Training and evaluation were done via a 5-fold cross-validation loop. Group-fold cross-validation was used to ensure that images of the same eye were always together in either training or test set. The

batch size was set to 16 for all models. The *Adam* optimizer was used with $lr = 0.001$ for segmentation. Models were trained for a fixed number of epochs across folds: 100 for vessel segmentation; 200 for A/V segmentation; 100 for disc segmentation and 35 for fovea localization. This was decided approximately based on experiments with a partition of 20% of the training set. We observed flat performance progression on these sets before and after the chosen epoch number and did not consider it necessary to do further optimization. Some architectural choices such as the use of deep supervision and increased UNet depth were validated using the same partition.

Per-fold models were trained on a cluster using a single NVidia graphics card per model. Segmentation models were trained in mixed precision.

0.4 Evaluation

We evaluated our models via 5-fold cross-validation, with the Dice score as the main evaluation metric. We report the mean scores (separated per source dataset) over the five validation sets. This is to provide a score of generalization performance on all datasets 1. For all models, we input pre-processed images in $1024 \times 1024 \text{px}$ resolution. Test-time augmentation was enabled. Note that this evaluation setup means that the scores of our models could be slightly under-represented when compared to the full ensemble of our models.

For the A/V model artery and vein masks were recovered from the model outputs. For the VaseX model, this meant merging the *Crossings* output mask with both *Artery* and *Vein* masks.

0.4.1 Quality evaluation

We made use of the Eye-Quality (EyeQ) Assessment Dataset [14] to train our quality evaluation model, which we used to assess the quality of the CFIs (Table 1). This dataset contains manual gradings of fundus quality using a 3-class system. CFIs were graded as one of: unusable/bad, usable and good quality. We took advantage of the ordinal nature of these classes to produce continuous quality scores from the outputs of our quality classification model:

1. Applied the Softmax function with a temperature parameter T to obtain probabilities:

$$p_i = \frac{e^{z_i/T}}{\sum_{j=1}^n e^{z_j/T}} \quad \text{for } i = 1, 2, \dots, n \quad (1)$$

where z_i is the logit corresponding to class i and $n = 3$; the number of classes.

2. Merged probabilities into a score by linearly combining the class indices and the probabilities:

$$S = \sum_{i=1}^n i \cdot p_i \quad (2)$$

This approach takes into account all logits to produce the final score. The value of T influences the sharpness of the probabilities and therefore how much the quality score is dominated by the largest logit. We tuned T manually to balance the sharpness and smoothness of the probability distribution of the resulting scores.

RESULTS

0.5 Comparison with publicly available models

We compared the performance of our models with that of publicly available ones. Note that our goal was not to compare deep learning architectures but instead to compare the performance of entire systems (including architecture, inference code, and public model weights) across different datasets (Table 1). Therefore architectures published without publicly available weights have been excluded from this analysis.

We compared the three segmentation models (vessels, artery-vein, disc) to the models in Automorph [40], the most comparable pipeline that integrates vessel, A/V, and disc segmentation. For each task, we compared against the corresponding model ensemble (7 models) in the Automorph pipeline. Additionally, we compared vessel and A/V models to Little-WNet (LWNet) [15], a dedicated vessel and A/V segmentation model with publicly available weights. The LWNET vessel segmentation weights were trained

Model	ChaseDB	DRHAGIS	HRF	RETA	FIVES	Leuven-Haifa	RS
Automorph	NA	.741	NA	NA	.824	.812	.810
LWNet	.732	.672	.573	NA	.756	.713	.745
VascX	.780	.769	.786	.890	.831	.829	.852

(a) Vessel segmentation (Dice score).

Model	HRF-AV		RITE		Les-AV		Leuven-Haifa		RS	
	A	V	A	V	A	V	A	V	A	V
Automorph [40]	NA	NA	NA	NA	NA	NA	.707	.773	.712	.752
LWNet [15]	.506	.574	NA	NA	.618	.670	.569	.649	.635	.696
VascX	.746	.792	.711	.760	.800	.835	.786	.826	.817	.849

(b) Artery-vein segmentation (Dice score). A: arteries mask score, V: veins mask score

Model	ORIGA	PAPILA	IDRiD	ADAM	PALM	REFUGE2	RS
Automorph	.876	.618	.931	.958	.846	NA	.220
VascX	.958	.961	.958	.964	.921	.956	.886

(c) Disc segmentation (Dice score)

Model	IDRID	ADAM	PALM	REFUGE2	RS
VascX	14.68	11.15	26.22	10.68	25.14

(d) Fovea localization (L2/Euclidean distance to ground truth in pixels)

Table 2. Performance comparison of VascX segmentation models. *NA* is used when the model was trained on the corresponding dataset and it is not possible to benchmark on out-of-distribution data.

on DRIVE. For A/V segmentation we tested both DRIVE and HRF-trained weights. We found DRIVE weights to perform better across all datasets and therefore report only these scores.

Table 2 shows the results of our comparison using Dice score (segmentation) and Euclidean distance (fovea localization) as evaluation metrics. In general, these results reveal higher performance from VascX across datasets and tasks.

Differences are smallest for the vessel segmentation task, where all models achieve consistently high Dice scores, suggesting that model performance in this task may be saturated for current architectures.

For A/V segmentation the VascX model achieved higher Dice scores across all datasets, with slightly higher performance for veins than for arteries, as has been observed in previous work. Importantly, we observed large improvements in Rotterdam Study and Leuven-Haifa datasets, the only ones evaluated across the three models (Figure 1). The differences was ~ 0.1 for the Rotterdam Study, the most diverse of the datasets; suggesting increased model robustness.

Regarding disc segmentation, the largest difference was in the Rotterdam Study, where Automorph achieved a score of only 0.220. It must be noted that some of the failure cases were due to Automorph’s bounds detection algorithm failing on RS CFIs. The disc detection was however also prone to fail for discs located close to or crossing the bounds of the CFI; and for images for which the disc border had low contrast. A large difference was also observed in PAPILA, which has a 30 degree field of view. The low performance of Automorph is likely partly from lack of 30-degree training samples when compared to VascX.

Qualitatively we observed a marked improvement in segmentation performance from VascX models. Figure 3 shows example model outputs from Rotterdam Study and Leuven-Haifa inputs (the two independent datasets). We observed more consistent disc detection from VascX, especially in cases where the disc was not clearly differentiated. A/V segmentation, while not flawless, produced visibly less continuity and mis-classification mistakes than both LWNNet and Automorph. Importantly, many of the vessel crossings were correctly resolved on both artery and vein masks.

0.6 Effect of image quality

To more deeply characterize the performance of the model, we made use of the CFI quality estimation model to classify Rotterdam Study images into *Good*, *Usable* and *Bad / Unusable* categories. We limited this analysis to the Rotterdam Study set due to the other dataset being smaller and/or highly uniform in terms of image quality and capture conditions. Figure 4a displays the distribution of Dice scores over image quality bins, as assessed by the model. Figure 4b shows the Dice score distributions for optic disc and macula-centered images. Once again vessel segmentation models achieved high consistency even for CFIs classified as *bad* quality. In A/V segmentation, *bad* images had lower performance. It stands out that the largest difference between VascX and the rest is in *usable* or intermediate quality images. Furthermore, it is clear that Automorph disc segmentation struggled with RS images, likely due to its more limited training set [40]. Performance was low for both disc and macula-centered images.

0.7 Feature accuracy

The goal of our models is to serve as the backbone for explainable feature extraction systems. Therefore, we compared retinal vascular features extracted from grader labels, Automorph segmentations, and VascX segmentations. Once again for VascX, we made use of segmentations of the test set for each fold to ensure out-of-distribution inference, and therefore the performance of our models might be under-represented. We made use of a feature extraction implementation used in previous work [27] for a set of 14 features including tortuosity and central retinal equivalents (CRE). All of these features make use of artery-vein segmentation, and some (CREs, temporal angles, vascular density) use disc segmentation and fovea location to define regions. Vessel segmentations were not used.

Table 3 shows the results, where it is clear that VascX produces features that are closer in magnitude and more highly correlated to the ground truth.

DISCUSSION

We presented new model ensembles for CFI vasculature analysis and benchmarked against publicly available systems. We developed the set of models in VascX with the objective of operating consistently across devices and achieving performance improvements on the diversity of images found on real cohort studies and clinical datasets. We augmented public datasets (which usually consist of carefully selected

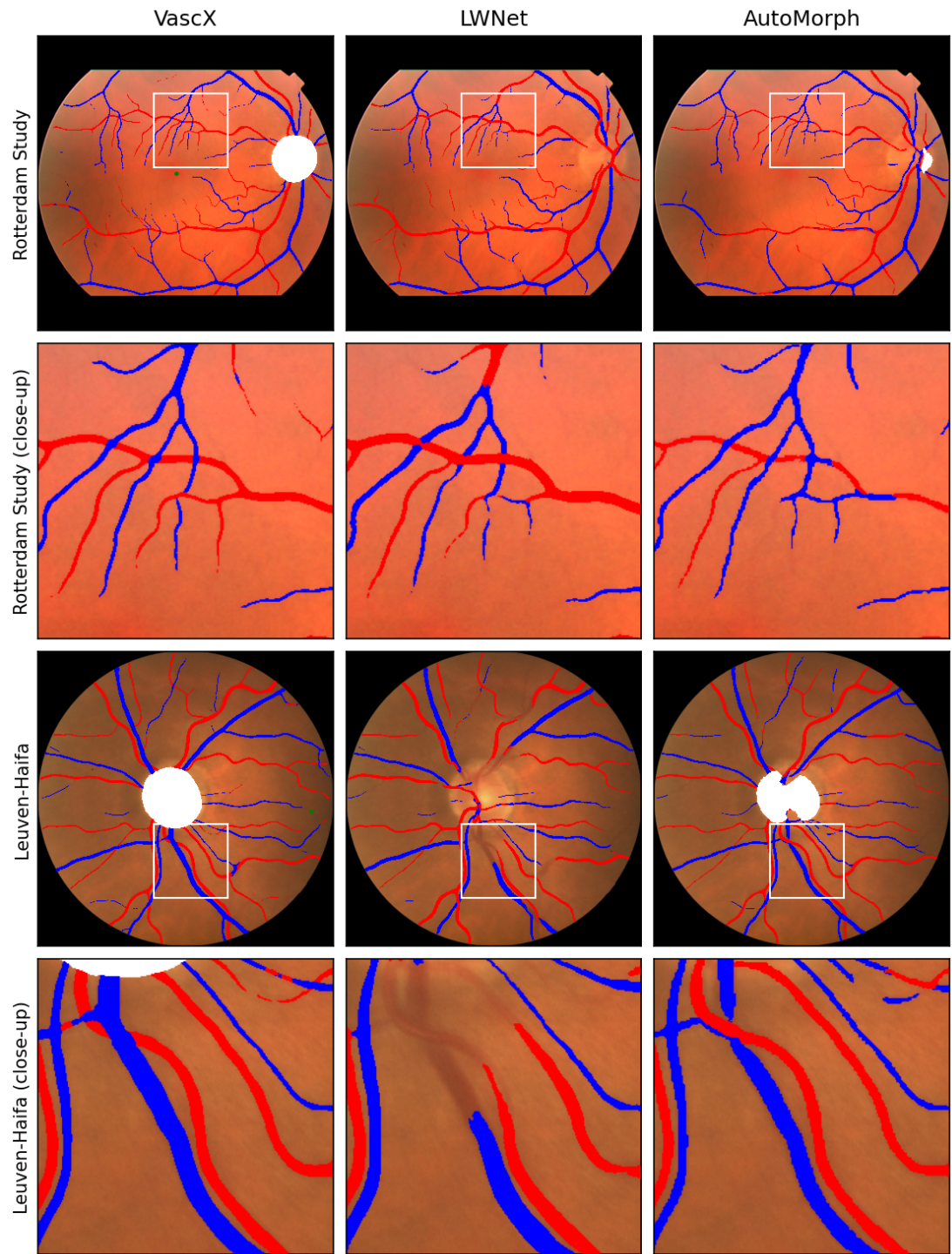


Figure 3. Example model outputs from the benchmarked systems showing A/V segmentation and disc and fovea outputs were applicable. We observed more consistency in A/V and disc segmentation from VascX. The CFIs shown correspond to the images with the median Dice score for A/V segmentation with VascX; for each dataset.

CFIs from one or a few devices) with Rotterdam Study CFIs collected throughout more than three decades from 11 different imaging devices and with diverse pathology. We made use of well-known architectures and strong augmentations to achieve solid performance across tasks.

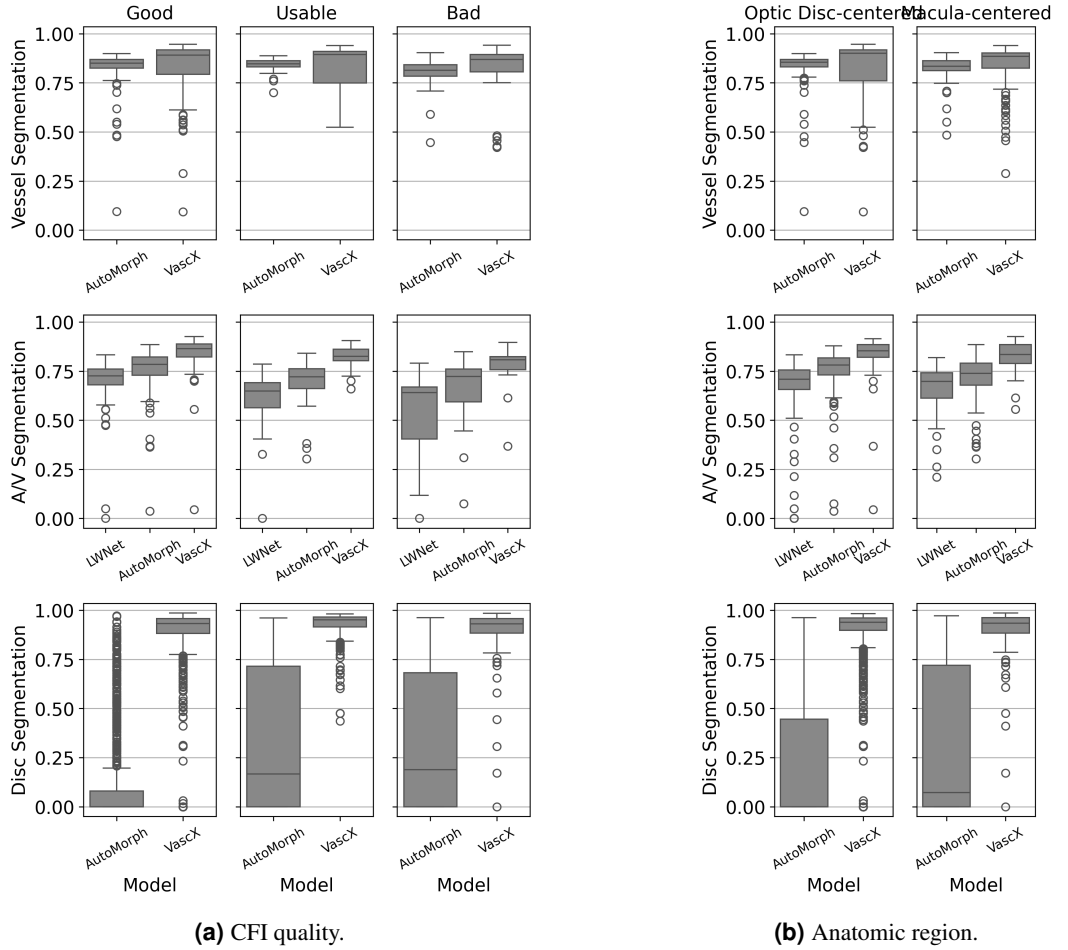


Figure 4. Box plots displaying the distribution of model performance (Dice score) over image quality and anatomic region (AR) bins/slices of the Rotterdam Study. For vessel segmentation, the performance of the models is stable across quality and anatomic region bins. For artery-vein segmentation, the biggest improvement is in *usable* images. For disc segmentation, the model achieves remarkably stable performance across image quality and AR; while the images pose a challenge for Automorph.

Our results show that our models outperform those in previous systems in every metric we evaluated. Our models achieve better segmentation performance across image quality levels and are similarly well-performing on disc and macula-centered images. We observed the largest performance improvement on A/V segmentation on CFIs of intermediate quality, likely common in large cohorts and many clinical datasets. Importantly, our models also outperformed Automorph and LWNNet models on the highest quality images. A large improvement was observed in disc segmentation performance when compared to Automorph, likely thanks to the greater image diversity on our augmented dataset. Finally, our results showed that better segmentation performance translates into better vascular features, in line with the results of Fhima et al. [10]. VascX features show lower absolute error and higher correlation with features extracted directly from grader segmentations.

Further work is required in several areas. There is room for improvement in artery-vein segmentation, especially regarding the connectivity of the vessel trees. Despite the improvements, our model still produces A/V misclassifications and gaps. Enforcing the expected tree structure in the segmentation is a notorious open challenge in deep learning. Incorporating specific loss functions and post-processing steps may provide improvements. However, the Dice score is not a metric suitable for the evaluation of connectivity. The development and evaluation of metrics that capture connectivity is therefore relevant in this line of work.

Classification of image quality using a one-dimensional image-level label, while useful, is not granular

	Grader μ	Mean Δ		Pearson r	
		Automorph	VascX	Automorph	VascX
Temporal Angle - A	120.848	6.435	4.625	0.673	0.760
Temporal Angle - V	127.208	6.070	4.089	0.701	0.822
CRE - A	10.223	1.529	0.989	0.699	0.854
CRE - V	15.455	2.005	1.150	0.777	0.880
Vasc. Density - A	0.055	0.013	0.006	0.693	0.865
Vasc. Density - V	0.063	0.010	0.005	0.762	0.894
Caliber median - A	2.908	0.667	0.593	0.666	0.668
Caliber std - A	1.829	0.380	0.278	0.612	0.795
Caliber median - V	2.928	0.636	0.590	0.728	0.675
Caliber std - V	2.382	0.431	0.250	0.691	0.883
Tortuosity - A	1.087	0.007	0.006	0.733	0.772
Tortuosity - V	1.086	0.006	0.005	0.568	0.690
Bifurcations - A	44.607	22.930	20.337	0.687	0.706
Bifurcations - V	51.107	23.690	22.693	0.757	0.791

Table 3. Comparison of features extracted from ground truth annotations and from VascX and Automorph segmentations on the Rotterdam Study artery-vein segmentation set (300 CFIs). Grader μ is the mean of the feature; mean Δ is the mean absolute error between ground truth features and features extracted from model outputs. Pearson coefficients are correlations between ground truth and model outputs.

enough for some applications. Artifacts or defocus, for example, may affect part of the image. A CFI that is unusable for vascular analysis may not be unusable for optic disc analysis, for example. Or a CFI may be usable for analysis of the main vascular arches but not the micro-vasculature.

We expect that VascX models will serve as the backbone for CFI vascular analysis, both in large cohort data and in smaller datasets. To this end, we expect that the ease of use of our *Pytorch* pipeline will aid researchers in efficiently obtaining segmentation and derived features. It is our objective that VascX catalyzes work toward understanding the statistical power of vascular analysis pipelines to expose signals in different kinds of data.

Furthermore, our vessel, disc, and fovea localization models may be useful beyond vascular where robust localization of these structures is required (eg. automatic ETDRS grid placement, or vessel-based quality estimation).

DATA SHARING

With this publication, we make available our model weights, training, and inference pipeline code.

- Our CFI preprocessing code is available at:
<https://github.com/Eyened/retinalysis-fundusprep>
- Our VascX models are available at:
https://github.com/Eyened/rtnls_vascx_models
This repository includes instructions to install our inference pipeline. This pipeline contains utilities to apply each model ensemble (from 5-fold cross-training) on external datasets, including applying the pre-processing steps.

ACKNOWLEDGMENTS

We acknowledge the Eyened team, and in particular the Reading Center, for their role in developing the algorithms. We acknowledge the Sinergia consortium for conceiving and supporting this project. This work was funded by the Swiss National Science Foundation grant no. CRSII5_209510.

REFERENCES

- [1] Muhammad Naseer Bajwa, Gur Amrit Pal Singh, Wolfgang Neumeier, Muhammad Imran Malik, Andreas Dengel, and Sheraz Ahmed. G1020: A benchmark retinal fundus image dataset for computer-aided glaucoma detection, 2020.
- [2] Attila Budai and Jan Odstrcilik. High resolution fundus (hrf) image database, 2013. URL <https://www5.cs.fau.de/research/data/fundus-images/>.
- [3] Wenting Chen, Shuang Yu, Kai Ma, Wei Ji, Cheng Bian, Chunyan Chu, Linlin Shen, and Yefeng Zheng. Tw-gan: Topology and width aware gan for retinal artery/vein classification. *Medical Image Analysis*, 77:102340, 2022. ISSN 1361-8415. doi: <https://doi.org/10.1016/j.media.2021.102340>.
- [4] C Cheung and TY Wong. Quantitative and qualitative retinal microvascular characteristics and blood pressure. *Journal of Hypertension*, 29:1380–1391, 2011. doi: [10.1097/HJH.0b013e328347266c](https://doi.org/10.1097/HJH.0b013e328347266c).
- [5] CYL Cheung, W Hsu, ML Lee, JJ Wang, P Mitchell, QP Lau, and TY Wong. A new method to measure peripheral retinal vascular caliber over an extended area. *Microcirculation*, 17:495–503, 2010. doi: [10.1111/j.1549-8719.2010.00048.x](https://doi.org/10.1111/j.1549-8719.2010.00048.x).
- [6] N Dervenis, AL Coleman, A Harris, MR Wilson, F Yu, E Anastasopoulos, and F Topouzis. Factors associated with retinal vessel diameters in an elderly population: The thessaloniki eye study. *Investigative Ophthalmology & Visual Science*, 60:2208–2217, 2019. doi: [10.1167/iovs.18-26276](https://doi.org/10.1167/iovs.18-26276).
- [7] H. Fang, F. Li, J. Wu, et al. Open fundus photograph dataset with pathologic myopia recognition and anatomical structure annotation. *Scientific Data*, 11:99, 2024. doi: [10.1038/s41597-024-02911-2](https://doi.org/10.1038/s41597-024-02911-2).
- [8] Huihui Fang, Fei Li, Huazhu Fu, Xu Sun, Xingxing Cao, Fengbin Lin, Jaemin Son, Sunho Kim, Gwenole Quelled, Sarah Matta, Sharath M. Shankaranarayana, Yi-Ting Chen, Chuen-Heng Wang, Nisarg A. Shah, Chia-Yen Lee, Chih-Chung Hsu, Hai Xie, Baiying Lei, Ujjwal Baid, Shubham Innani, Kang Dang, Wenxiu Shi, Ravi Kamble, Nitin Singhal, Ching-Wei Wang, Shih-Chang Lo, Jose Ignacio Orlando, Hrvoje Bogunovic, Xiulan Zhang, and Yanwu Xu. Adam challenge: Detecting age-related macular degeneration from fundus images. *IEEE Transactions on Medical Imaging*, 41(10):2828–2847, October 2022. ISSN 1558-254X. doi: [10.1109/tmi.2022.3172773](https://doi.org/10.1109/tmi.2022.3172773). URL <http://dx.doi.org/10.1109/TMI.2022.3172773>.
- [9] Huihui Fang, Fei Li, Junde Wu, Huazhu Fu, Xu Sun, Jaemin Son, Shuang Yu, Menglu Zhang, Chenglang Yuan, Cheng Bian, Baiying Lei, Benjian Zhao, Xinxing Xu, Shaohua Li, Francisco Fumero, José Sigut, Haidar Almubarak, Yakoub Bazi, Yuanhao Guo, Yating Zhou, Ujjwal Baid, Shubham Innani, Tianjiao Guo, Jie Yang, José Ignacio Orlando, Hrvoje Bogunović, Xiulan Zhang, and Yanwu Xu. Refuge2 challenge: A treasure trove for multi-dimension analysis and evaluation in glaucoma screening, 2022. URL <https://arxiv.org/abs/2202.08994>.
- [10] J. Fhima, J. Van Eijgen, M. I. Billen Moulin-Romsée, et al. Lunet: deep learning for the segmentation of arterioles and venules in high resolution fundus images. *Physiological Measurement*, 45(5): 10.1088/1361-6579/ad3d28, 2024. doi: [10.1088/1361-6579/ad3d28](https://doi.org/10.1088/1361-6579/ad3d28). Published 2024 May 3.
- [11] Muhammad Moazam Fraz, Paolo Remagnino, Andreas Hoppe, Bunyarit Uyyanonvara, Alicja R. Rudnicka, Christopher G. Owen, and Sarah A. Barman. Chase db1: Retinal vessel reference dataset, 2012. URL <https://researchdata.kingston.ac.uk/96/>.
- [12] S Frost, Y Kanagasingam, SL Macaulay, et al. Retinal vascular biomarkers for early detection and monitoring of alzheimer’s disease. *Translational Psychiatry*, 3:e233, 2013.
- [13] Huazhu Fu, Fei Li, José Ignacio Orlando, Hrvoje Bogunović, Xu Sun, Jingan Liao, Yanwu Xu, Shaochong Zhang, and Xiulan Zhang. Refuge: Retinal fundus glaucoma challenge, 2019. URL <https://dx.doi.org/10.21227/tz6e-r977>.
- [14] Huazhu Fu, Boyang Wang, Jianbing Shen, Shanshan Cui, Yanwu Xu, Jiang Liu, and Ling Shao. *Evaluation of Retinal Image Quality Assessment Networks in Different Color-Spaces*, page 48–56. Springer International Publishing, 2019. ISBN 9783030322397. doi: [10.1007/978-3-030-32239-7_6](https://doi.org/10.1007/978-3-030-32239-7_6). URL http://dx.doi.org/10.1007/978-3-030-32239-7_6.

- [15] Adrian Galdran, André Anjos, José Dolz, Hadi Chakor, Hervé Lombaert, and Ismail Ben Ayed. The little w-net that could: State-of-the-art retinal vessel segmentation with minimalistic models, 2020.
- [16] S. Holm, G. Russell, V. Nourrit, and N. McLoughlin. Dr hagsis - a fundus image database for the automatic extraction of retinal surface vessels from diabetic patients. *J Med Imaging (Bellingham)*, 4 (1):014503, Jan 2017. doi: 10.1117/1.JMI.4.1.014503. Epub 2017 Feb 9.
- [17] LD Hubbard, RJ Brothers, WN King, et al. Methods for evaluation of retinal microvascular abnormalities associated with hypertension/sclerosis in the atherosclerosis risk in communities study. *Ophthalmology*, 106(12):2269–2280, 1999.
- [18] M. A. Ikram, G. Brusselle, M. Ghanbari, et al. Objectives, design and main findings until 2020 from the rotterdam study. *European Journal of Epidemiology*, 35:483–517, 2020. doi: 10.1007/s10654-020-00640-5.
- [19] Fabian Isensee, Paul F Jaeger, Simon A Kohl, Jens Petersen, and Klaus H Maier-Hein. nnu-net: a self-configuring method for deep learning-based biomedical image segmentation. *Nature methods*, 18(2):203–211, 2021.
- [20] A Iwase, A Sekine, J Suehiro, K Tanaka, Y Kawasaki, R Kawasaki, and M Araie. A new method of magnification correction for accurately measuring retinal vessel calibers from fundus photographs. *Investigative Ophthalmology & Visual Science*, 58:1858–1864, 2017. doi: 10.1167/iovs.16-21202.
- [21] K. Jin, X. Huang, J. Zhou, et al. Fives: A fundus image dataset for artificial intelligence based vessel segmentation. *Sci Data*, 9:475, 2022. doi: 10.1038/s41597-022-01564-3.
- [22] R Klein, CE Myers, MD Knudtson, KE Lee, R Gangnon, TY Wong, and BE Klein. Relationship of blood pressure and other factors to serial retinal arteriolar diameter measurements over time: The beaver dam eye study. *Archives of Ophthalmology*, 130:1019, 2012. doi: 10.1001/archophthamol.2012.560.
- [23] O. Kovalyk, J. Morales-Sánchez, R. Verdú-Monedero, et al. Papila: Dataset with fundus images and clinical data of both eyes of the same patient for glaucoma assessment. *Sci Data*, 9:291, 2022. doi: 10.1038/s41597-022-01388-1.
- [24] G Liew, JJ Wang, P Mitchell, and TY Wong. Retinal vascular imaging: a new tool in microvascular disease research. *Circulation: Cardiovascular Imaging*, 1(2):156–161, 2008.
- [25] Xiang Lyu, Li Cheng, and Shuo Zhang. The reta benchmark for retinal vascular tree analysis. *Scientific Data*, 9:397, 2022. doi: 10.1038/s41597-022-01507-y.
- [26] José Ignacio Orlando, João Barbosa Breda, Karel van Keer, Matthew B. Blaschko, Pablo J. Blanco, and Carlos A. Bulant. Towards a glaucoma risk index based on simulated hemodynamics from fundus images. In Alejandro F. Frangi, Julia A. Schnabel, Christos Davatzikos, Carlos Alberola-López, and Gabor Fichtinger, editors, *Medical Image Computing and Computer Assisted Intervention – MICCAI 2018*, pages 65–73, Cham, 2018. Springer International Publishing. ISBN 978-3-030-00934-2.
- [27] Sofía Ortín Vela, Michael Johannes Beyeler, Olga Trofimova, Mattia Tomasoni, Ilaria Iuliani, David Presby, Florence Hoogewoud, and Sven Bergmann. Phenotypic and genetic characteristics of retinal vascular parameters and their association with diseases. *medRxiv*, 2023. doi: 10.1101/2023.07.07.23292368.
- [28] JC Parr and GF Spears. General caliber of the retinal arteries expressed as the equivalent width of the central retinal artery. *American Journal of Ophthalmology*, 77(4):472–477, 1974.
- [29] A Perez-Rovira, T MacGillivray, E Trucco, KS Chin, K Zutis, C Lupascu, and B Dhillon. Vampire: Vessel assessment and measurement platform for images of the retina. In *2011 Annual International Conference of the IEEE Engineering in Medicine and Biology Society*, pages 3391–3394. IEEE, 2011. doi: 10.1109/IEMBS.2011.6090918.

- [30] Prasanna Porwal, Samiksha Pachade, Ravi Kamble, Manesh Kokare, Girish Deshmukh, Vivek Sahasrabudde, and Fabrice Meriaudeau. Indian diabetic retinopathy image dataset (idrid), 2018. URL <https://dx.doi.org/10.21227/H25W98>.
- [31] Touseef Ahmad Qureshi, Maged Habib, Andrew Hunter, and Bashir Al-Diri. A manually-labeled, artery/vein classified benchmark for the drive dataset. In *Proceedings of the 26th IEEE International Symposium on Computer-Based Medical Systems*, pages 485–488, 2013. doi: 10.1109/CBMS.2013.6627847.
- [32] Joes Staal, Michael D Abramoff, Meindert Niemeijer, Max A Viergever, and Bram Van Ginneken. Ridge-based vessel segmentation in color images of the retina. *IEEE transactions on medical imaging*, 23(4):501–509, 2004.
- [33] E Trucco, L Ballerini, D Relan, A Giachetti, T MacGillivray, K Zutis, and B Dhillon. Novel vampire algorithms for quantitative analysis of the retinal vasculature. In *Proceedings of the 2013 ISSNIP Biosignals and Biorobotics Conference: Biosignals and Robotics for Better and Safer Living (BRC)*, pages 1–4. IEEE, 2013. doi: 10.1109/BRC.2013.6487501.
- [34] E Trucco, A Giachetti, L Ballerini, D Relan, A Cavinato, and TJ MacGillivray. Morphometric measurements of the retinal vasculature in fundus images with vampire. In F Karray and A de Albuquerque Araujo, editors, *Biomedical Image Understanding: Methods and Applications*, pages 253–274. John Wiley & Sons, Hoboken, NJ, USA, 2015.
- [35] Jan Van Eijgen, Jonathan Fhima, Marie-Isaline Billen Moulin-Romsée, Joachim A. Behar, Eirini Christinaki, and Ingeborg Stalmans. Leuven-haifa high-resolution fundus image dataset for retinal blood vessel segmentation and glaucoma diagnosis. *Scientific Data*, 11(1):257, February 2024. ISSN 2052-4463. doi: 10.1038/s41597-024-03086-6. URL <https://doi.org/10.1038/s41597-024-03086-6>.
- [36] FF Wei, ZY Zhang, T Petit, N Cauwenberghs, YM Gu, L Thijs, and JA Staessen. Retinal microvascular diameter, a hypertension-related trait, in ecg-gated vs. non-gated images analyzed by ivan and siva. *Hypertension Research*, 39:886–892, 2016. doi: 10.1038/hr.2016.81.
- [37] TY Wong, R Klein, BEK Klein, et al. Retinal vessel diameters and their associations with age and blood pressure. *Investigative Ophthalmology & Visual Science*, 43(7):2859–2864, 2002.
- [38] TY Wong, FMA Islam, R Klein, BE Klein, MF Cotch, C Castro, and E Shahar. Retinal vascular caliber, cardiovascular risk factors, and inflammation: The multi-ethnic study of atherosclerosis (mesa). *Investigative Ophthalmology & Visual Science*, 47:2341–2350, 2006. doi: 10.1167/iovs.05-1539.
- [39] Z. Zhang, F.S. Yin, J. Liu, W.K. Wong, N.M. Tan, B.H. Lee, J. Cheng, and T.Y. Wong. Origa(-light): an online retinal fundus image database for glaucoma analysis and research. In *2010 Annual International Conference of the IEEE Engineering in Medicine and Biology*, pages 3065–3068. IEEE, 2010. doi: 10.1109/IEMBS.2010.5626137.
- [40] Yukun Zhou, Siegfried K. Wagner, Mark A. Chia, An Zhao, Peter Woodward-Court, Moucheng Xu, Robbert Struyven, Daniel C. Alexander, and Pearse A. Keane. AutoMorph: Automated Retinal Vascular Morphology Quantification Via a Deep Learning Pipeline. *Translational Vision Science & Technology*, 11(7):12–12, 07 2022. ISSN 2164-2591. doi: 10.1167/tvst.11.7.12. URL <https://doi.org/10.1167/tvst.11.7.12>.

A DATASET DETAILS

Table 4. Complementary details of the public dataset used in model development.

Dataset	N	Resolution	Devices
Vessel Segmentation			
Chase DB [11]	28	35°, 1280 × 960	Nidek NM-200-D
DRHAGIS [16]	40	45°, 4752 × 3168 – 2816 × 1880	Topcon TRC-NW6s, Topcon TRC-NW8, Canon CR DGi
HRF [2]	45	45°, 3504 × 2336	NR
RETA [25]	54	50°, 4288 × 2848	Kowa VX-10 alpha
FIVES [21]	800	50°, 2048 × 2048	Topcon TRC-NW8
Leuven-Haifa [35]	240	1444 × 1444	Zeiss Visucam 500
RS (ours)	352		see Fig. 1
Total	1559		
Artery Vein Segmentation			
RITE [31]	40	45°, 768 × 584	Canon CR5 3CCD
HRF-AV [3]	45	45°, 3504 × 2336	NR
Les-AV [26]	22	30°, 1444 × 1620	NR
Leuven-Haifa [35]	240	30°, 1444 × 1444	Zeiss Visucam 500
RS (ours)	215		see Fig. 1
Total	562		
Disc Segmentation			
ORIGA [39]	650	NR	NR
PAPILA [23]	488	45°, 2576 × 1934	Topcon TRC-NW400
IDRiD [30]	81	50°, 4288 × 2848	Kowa VX-10 alpha
ADAM [8]	821*	2124 × 2056, 1444 × 1444	Zeiss Visucam 500, Canon CR-2
PALM [7]	1179**	2124 × 2056, 1444 × 1444	Zeiss Visucam 500, Canon CR-2
REFUGE2 [13]	2000	1634 × 1634 - 2124 × 2056	Zeiss Visucam 500, Canon CR-2, Topcon TRC-NW400, Kowa
RS (ours)	1225		see Fig. 1
Total	7464		
Fovea Localization			
IDRiD [30]	516	50°, 4288 × 2848	Kowa VX-10 alpha
ADAM [8]	1200	2124 × 2056, 1444 × 1444	Zeiss Visucam 500, Canon CR-2
PALM [7]	1200	2124 × 2056, 1444 × 1444	Zeiss Visucam 500, Canon CR-2
REFUGE2 [13]	2000	1634 × 1634 - 2124 × 2056	Zeiss Visucam 500, Canon CR-2, Topcon TRC-NW400, Kowa
RS (ours)	10908		see Fig. 1
Total	15824		
CFI Quality Estimation			
EyeQ [14]	28,792		